ATLAS NOTE

ATLAS-CONF-2016-053

3rd August 2016

Search for heavy neutral resonances in vector boson fusion in pp collisions at $\sqrt{s} = 13$ TeV with the ATLAS detector at the Large Hadron Collider

The ATLAS Collaboration

Abstract

This note presents a search for new heavy neutral resonances (R) produced through vector boson fusion process $qq \to Rqq \to \ell^+\nu\ell^-\bar{\nu}qq$ ($\ell = e, \mu$) using 3.2 fb^{-1} of data at $\sqrt{s} = 13$ TeV recorded by the ATLAS detector at the Large Hadron Collider. No excess above the Standard Model background expectation is observed. Limits are set on the production of five types of neutral resonances of different spin and isospin quantum numbers (scalar isoscalar, scalar isotensor, vector isovector, tensor isoscalar and tensor isotensor) with a K-matrix unitarization of the vector boson scattering process.

1 Introduction

The process of vector boson scattering can be sensitive to phenomena beyond the standard model (SM), in particular the presence of diboson resonances and anomalous quartic couplings. Resonances of different spin and isospin quantum numbers are generically predicted in composite Higgs models [1, 2], triplet Higgs models [3–5], and extra dimension models [6, 7]. Cross sections and branching ratios of the 125 GeV scalar boson discovered at the Large Hadron Collider (LHC) are presently compatible, within experimental precision, with those predicted for the SM Higgs boson. However, if the values of the Higgs coupling to the vector bosons do not take the exact values predicted by the SM, an alternative mechanism is needed to restore unitarity in the scattering amplitude of longitudinal gauge bosons, and new resonances may appear [8–12]. If these resonances have weak or no coupling to fermions, vector boson scattering processes could provide the best sensitivity to these resonance searches at the LHC.

In this search, a benchmark model is used which combines new resonances of different spin and isospin quantum numbers with an effective chiral Lagrangian (EChL) [13–17]. These resonances are assumed to only couple to longitudinal vector bosons and do not couple to fermions, photons and transverse components of vector bosons. The resonance decay widths shown in Table 1 are calculated according to Ref. [15]. These resonances contribute additional terms to the scattering amplitudes and are associated with anomalous quartic gauge couplings implying a violation of unitarity. These effects are evaluated in the EChL model and a unitarization procedure is required, as in Refs. [10, 14–17]. Here, a K-matrix unitarization procedure [14] is used. The EChL gathers three gauge bosons ω^a ($a = 1, 2, 3$) in a matrix which transforms in an $SU(2)_L \times U(1)_Y$ invariant way and the Higgs boson is included in a nonlinear representation.

ATLAS [18] and CMS [19] have provided evidence for the Higgs boson production via the $qq \to Hqq \to W^+W^-qq \to \ell^+\nu\ell^-\bar{\nu}qq$ fusion process using 7 and 8 TeV data. ATLAS also searched for a charged Higgs boson, $H^\pm$, produced via vector-boson fusion and decaying to a W boson and a Z boson using 8 TeV data [20]. In this note, a search is performed for the first time for neutral resonances above the Higgs boson mass produced by the $qq \to Rqq \to \ell^+\nu\ \ell^-\bar{\nu}\ qq$ ($\ell = e, \mu$) fusion process, taking into account interference with the SM production process of the same final state, and applying a K-matrix unitarization. A representative Feynman diagram of the production and decay of the resonance is shown in Figure 1. Only leptonic channels are considered due to the relatively small SM backgrounds expected. Three channels are labeled based on the lepton flavors: ee, $e\mu$, and $\mu\mu$. The analysis is based on an integrated luminosity of 3.2 fb^{-1} of proton-proton collision data taken at $\sqrt{s} = 13$ TeV in 2015.

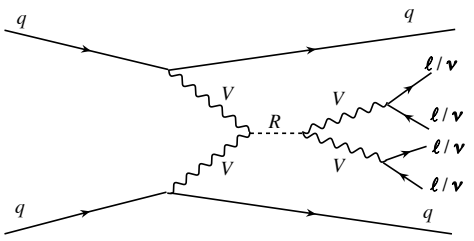

Figure 1: Representative Feynman diagram for the production and decay of a heavy neutral resonance (R) by vector boson fusion at the LHC. The symbol q represents all possible quarks or anti-quarks, and V represents W or Z boson.

Type	Spin J	Isospin I	Electric Charge	Γ/Γ_0
σ	0	0	0	6
ϕ	0	2	$--, -, 0, +, ++$	1
ρ	1	1	$-, 0, +$	$\frac{4}{3}(\frac{\upsilon^2}{m^2})$
f	2	0	0	$\frac{1}{5}$
t	2	2	$--, -, 0, +, ++$	$\frac{1}{30}$

Table 1: Spin, isospin and corresponding electric charge for five types of resonances. Only neutral resonances are considered. The last column gives the relative width Γ/Γ_0 where $\Gamma_0 = g^2m^3/64\pi\upsilon^2$ with g as the coupling of the new resonance to the longitudinal vector bosons [15], m as the mass of the resonance, and υ as the electroweak scale of 246 GeV.

2 ATLAS Detector

The ATLAS detector [21] is a multi-purpose particle physics apparatus with a forward-backward symmetric cylindrical geometry and almost 4π coverage in solid angle[1]. The inner tracking detector (ID) covers $|\eta| < 2.5$ in pseudorapidity and consists of a silicon pixel detector, a silicon microstrip detector, and a transition radiation tracker. The ID is surrounded by a superconducting solenoid providing a 2 T magnetic field and by a hermetic, finely-segmented calorimeter system covering $|\eta| < 4.9$, which provides three-dimensional reconstruction of particle showers using lead-liquid argon sampling for the electromagnetic compartment followed by a hadronic compartment which is based on iron-scintillating tiles sampling in the central region and on liquid argon sampling with copper or tungsten absorbers for $|\eta| > 1.7$. The muon spectrometer (MS) has one barrel and two endcap air-core toroids that bend muons. Three layers of precision tracking stations, consisting of drift tubes and cathode strip chambers, allow precise muon momenta to be measured up to $|\eta| = 2.7$. Resistive plate and thin-gap chambers provide muon triggering capability up to $|\eta| = 2.4$.

3 Data and Simulated Events

The data were recorded with the ATLAS detector during the 2015 run and correspond to a total integrated luminosity of 3.2 fb^{-1} at a center-of-mass energy of 13 TeV. They are required to satisfy a number of conditions ensuring that the ATLAS detector was operating nominally. Events are selected if they satisfied at least one of a set of single electron or muon triggers with p_{T} thresholds of 24 GeV for the electron and 20 GeV for the muon.

Simulated Monte Carlo (MC) signal samples, $qq \to \ell^+\nu\ell^-\bar{\nu}qq$ ($\ell = e, \mu$), including a new resonance, the contribution from the SM electroweak processes that produce the same final state, and the interference between the SM and the new resonance, are generated with the Whizard generator v2.1.1 [22, 23]. The program Pythia8.186 [24] with the CTEQ6L1 [25] parton distribution function (PDF) set and A14 tune [26]

[1] ATLAS uses a right-handed coordinate system with its origin at the nominal interaction point (IP) in the centre of the detector and the z-axis along the beam pipe. The x-axis points from the IP to the centre of the LHC ring, and the y-axis points upward. Cylindrical coordinates (r, ϕ) are used in the transverse plane, ϕ being the azimuthal angle around the beam pipe. The pseudorapidity is defined in terms of the polar angle θ as $\eta = -\ln\tan(\theta/2)$. Transverse momentum ($p_{\mathrm{T}}$) is defined relative to the beam axis.

are used for parton shower and hadronization. The factorization scale (μ_F) and the renormalization scale (μ_R) are set to $\mu_F = \mu_R = 2m_W$, where m_W is the mass of the W boson. Events with W or Z bosons decaying to τ lepton that resulting in the ee, $e\mu$ or $\mu\mu$ final state are also included in the signal generation. Using the SM_km process model in Whizard, five types of new neutral resonance, as shown in Table 1, are produced: scalar isoscalar (σ), scalar isotensor (ϕ), vector isovector (ρ), tensor isoscalar (f) and tensor isotensor (t). Resonance masses ranging from 200 GeV to 500 GeV in steps of 100 GeV are produced. The coupling of the resonance to longitudinal vector bosons is set to $g = 2.5$. A preselection is applied on the event generation requiring the transverse momentum of jets and leptons to be greater than 15 GeV, the distance between the outgoing quarks in the $\eta - \phi$ plane to be $\Delta R_{qq'} \equiv \sqrt{(\phi_q - \phi_{q'})^2 + (\eta_q - \eta_{q'})^2} > 1.0$, and the invariant mass of the two leptons to be $m_{\ell\ell} > 10$ GeV. The vector bosons from the resonance decay are required to be on-shell, thus excluding the s-channel Higgs boson exchange contribution, where $H \to WW^*$ and $H \to ZZ^*$.

The signal cross section is defined here formally as the difference in the cross section obtained for the full MC samples of $qq \to Rqq \to \ell^+\nu\ell^-\bar{\nu}qq$ (which includes the new resonance, the SM background processes producing the same final state, and the interference between the SM and the new resonance) and that of the pure electroweak sample $qq \to \ell^+\nu\ell^-\bar{\nu}qq$, also generated with Whizard. The signal kinematic distributions are also obtained from the corresponding distribution difference between these two samples. The signal production cross section thus excluding the SM electroweak processes is shown for the five different resonance types as a function of the resonance mass in Figure 2. For σ resonances above 500 GeV, the ratio of the decay width to the resonance pole mass (Γ/m) reaches around 50% for a chosen coupling of $g = 2.5$ [16]. For higher masses the definition of a resonance is difficult due to the large decay width, thus only resonances with mass below 500 GeV are considered.

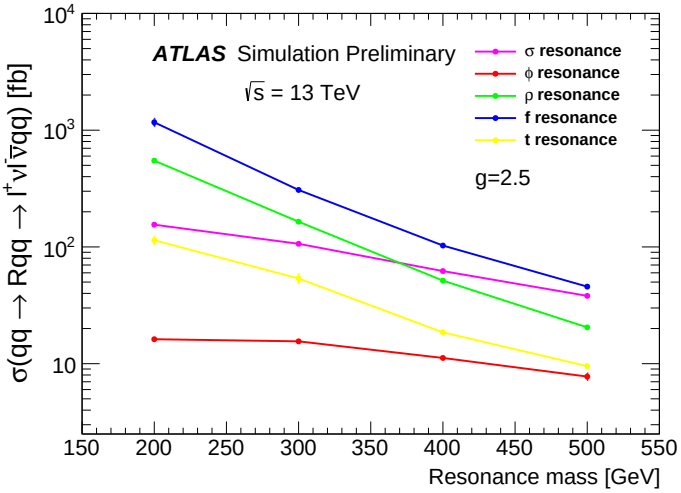

Figure 2: Production cross section times branching ratio of the signal process as a function of the resonance mass for all five different resonance types and with coupling parameter $g = 2.5$. The SM continuum contribution is subtracted.

SM background processes include those that lead to a final state with two opposite-sign prompt leptons and at least two jets, such as $t\bar{t}$, Z+jets, diboson, and Higgs production. Their contributions are estimated using simulated events. In all samples, W and Z bosons are allowed to decay to all three leptonic channels.

Both $t\bar{t}$ and single top quark production samples are generated with Powheg-Box v2 [27] using CT10

PDF [28] at Next-to-Leading Order (NLO) and showering is simulated with Pythia6.428 [29]. The cross sections are normalized to the Next-to-Next-to-Leading Order (NNLO) calculation including soft-gluon resummation to Next-to-Next-to-Leading-Logarithm order (NNLL) using a k-factor [30]. The $t\bar{t} + W/Z$ samples are generated using Madgraph v2.2.2 [31] with NNPDF23LO PDF set [32], with parton showering and hadronization with Pythia6.428, and are normalized to the NLO calculations with k-factors [33].

The $Z(\rightarrow \ell^+\ell^-)$+jets QCD production is generated with Madgraph v2.2.2 at LO with the parton shower and hadronization performed by Pythia8.186. The A14 tune is used together with the NNPDF23LO PDF set. Events with up to four partons at the parton level are generated. The cross section is normalized to the NNLO calculation [34–36]. The $Z(\rightarrow \ell^+\ell^-)$+jets production where pairs of jets result from the decay of a vector boson, is generated with Sherpa2.1.1 [37] with CT10 PDF at LO.

The $W^+(\rightarrow \ell^+\nu)W^-(\rightarrow \ell^-\bar{\nu})jj$ and other diboson processes in association with jets, $WZjj$, $ZZjj$ and $Z\gamma jj$, produced by QCD diagrams ($O(\alpha_s^2\alpha^2)$) and where the vector bosons decay leptonically, are modelled with Sherpa2.1.1 with CT10 PDF at LO, and normalized to NLO [38, 39]. The production of the $WWjj$ process by electroweak diagrams ($O(\alpha^4)$), including vector boson scattering, is generated with Whizard v2.1.1, as mentioned above. The contribution of electroweak diagrams to the other diboson processes is estimated to be negligible.

Simulation of Higgs production by gluon fusion ($gg \rightarrow H(\rightarrow WW^* \rightarrow \ell\nu\ell\nu)$), denoted as ggH, and by vector boson fusion ($qq' \rightarrow qq'H(\rightarrow WW^* \rightarrow \ell\nu\ell\nu)$) are generated with Powheg-Box v2 at NLO, using CT10 PDF, and interfaced with Pythia8.186 for partons shower and hadronization. The contributions of the $H \rightarrow ZZ^*$ process from both gluon fusion and vector boson fusion are found to be negligible.

All simulated MC samples include the effect of multiple interactions (pile-up) in the same and neighbouring proton bunch crossings by the addition of simulated diffractive and non-diffractive pp collisions to each generated signal or background event. The pile-up rate in MC simulation is weighted to reproduce the measured pile-up rate in data. Finally, all generated samples are processed through the Geant4-based ATLAS detector simulation [40, 41] and reconstructed with the standard ATLAS reconstruction software used for collision data.

4 Object and Event Selection

Due to the presence of pile-up, each event can have multiple vertices reconstructed. Only events where the primary vertex has at least three associated tracks with $p_T > 400$ MeV are considered. The vertex with the largest Σp_{T}^2 of associated tracks is denoted as the primary vertex.

Electrons are reconstructed from clusters of energy deposits in the EM calorimeter that match a track reconstructed in the ID. They are identified using a maximum likelihood procedure described in [42]. The levels referred as “loose”, “medium” and “tight” identification criteria, correspond to approximately 96%, 94% and 88% identification efficiency for electrons with transverse energy of 100 GeV. Track and calorimeter cluster isolation conditions are applied, based on the total p_{T} of tracks and calorimeter energy deposits around the electron track and cluster, within a cone radius of 0.2. The electrons are required to originate from the primary vertex, to satisfy the “tight” isolation requirements [43], and to have transverse momentum $p_{\mathrm{T}} > 25$ GeV and pseudorapidity $|\eta| < 2.47$, with a veto in the range $1.37 < |\eta| < 1.52$ which corresponds to the crack region between the barrel and endcap LAr calorimeters.

Muons are reconstructed by matching tracks in the inner detector and muon spectrometer. The quality criteria are defined in Ref. [44]. The muon is removed from the event if a jet with number of associated tracks greater than two is found within $\Delta R < 0.4$ of the muon candidate. Candidate muons are required to originate from the primary vertex, satisfy the "medium" identification criteria and "tight" isolation requirements [44], and to have transverse momentum $p_{\mathrm{T}} > 25$ GeV and $|\eta| < 2.5$.

To improve the agreement between data and simulation, lepton selection efficiencies are measured using dedicated samples of data and simulation, and correction factors are applied to the simulation to account for differences with respect to data. The simulation is tuned to reproduce the calorimeter energy and the muon momentum scale and resolution observed in data.

Jets are reconstructed using the anti-k_t algorithm [45] with a radius parameter of $R = 0.4$, using calorimeter clusters as input. The three-dimensional clusters are built from topologically connected calorimeter cells that contain a significant signal above noise and the energy scale of the jets is calibrated to the hadronic scale as in Ref. [46]. The clusters are corrected for dead material and out-of-cluster energy losses. To remove poorly reconstructed jets, jet cleaning criteria as well as area-based pile-up subtraction and the in-situ calibration corrections are applied [47]. A jet vertex tagger (JVT) [48] is a likelihood variable employed to tag and suppress pile-up jets, having a large fraction of tracks not associated with the primary vertex. Jets are required to have $p_{\mathrm{T}} > 30$ GeV and $|\eta| < 4.5$. Jets containing b-hadrons ("b-jet") with $|\eta| < 2.5$ are identified by combining information on the impact parameter significances of their tracks and explicit secondary vertex reconstruction [48]. The ATLAS jet flavor tagging algorithm, MV2c20 [49], with an efficiency of 85% for tagging $b-$jets in a MC sample of $t\bar{t}$ events, is used. Since electrons are also reconstructed as jets, if a reconstructed jet lies within $R = 0.2$ of an electron, it is discarded.

Due to the presence of two neutrinos in the final state, the missing transverse energy, $E_{\mathrm{T}}^{\mathrm{miss}}$, is an important discriminating variable for signal events. It is calculated as the negative of the sum of 4-vectors of energy clusters or track momenta from reconstructed objects such as electrons, muons, and jets. Photons and hadronically decaying taus are included as jets in the reconstruction. Tracks not associated to these hard objects are also taken into account as the track soft term.

Preselection cuts are applied on all signal and background MC samples. At least two leptons are required with $p_{\mathrm{T}} > 25$ GeV. At least one of the two leptons is required to be geometrically matched to a lepton reconstructed by the trigger algorithm. For the ee channel, at least one of them is required to pass the "medium" identification criteria, as defined in Ref. [42] . For the $e\mu$ channel, the electron needs to pass the "loose" identification criteria. The vector boson scattering signal process contains two forward tag jets, which could be contaminated by pile-up jets. To suppress pile-up effect, a higher p_{T} threshold of 50 GeV is set for jets which fall in $|\eta| > 2.5$.

Candidate events have a distinct experimental signature of exactly two high p_{T} leptons (electrons or muons), missing transverse energy ($E_{\mathrm{T}}^{\mathrm{miss}}$), and at least two forward jets. Kinematic selection criteria used in the final signal region are listed in Table 2. Candidate events are required to have exactly two opposite-sign leptons passing the above selection criteria with $m_{\ell\ell} > 40$ GeV. The dilepton invariant mass must not be within 25 GeV of the Z boson mass to reduce Z+jets background for both ee and $\mu\mu$ channels. Events are also required to have $E_{\mathrm{T}}^{\mathrm{miss}} > 35$ GeV. In order to reduce the top quark pair and single top quark background, events must not contain any b-jet. In addition, the two jets must have an invariant mass m_{jj} that is greater than 500 GeV and large separation in pseudorapidities ($|\Delta\eta_{jj}| > 2.4$). They are also required to be present in the opposite sides of the detector ($\eta_{j_1} \times \eta_{j_2} < 0$). To reduce the background from strong production of double vector boson processes, the lepton centrality is required to

#	Selection criteria
1	event preselection requirements, see text
2	exactly two leptons with $p_{\mathrm{T}} > 25$ GeV
3	pass single lepton trigger and trigger matching
4	third lepton veto
5	dilepton mass $m_{\ell\ell} > 40$ GeV
6	$q_{\ell_1} \times q_{\ell_2} < 0$
7	$\lvert m_{\ell\ell} - m_Z \rvert > 25$ GeV in the ee and $\mu\mu$ channels
8	at least two selected jets with $p_T > 30$ (50) GeV and $\lvert\eta\rvert < 2.5$ ($2.5 < \lvert\eta\rvert < 4.5$)
9	b-jet veto
10	$E_{\mathrm{T}}^{\mathrm{miss}} > 35$ GeV
11	$m_{jj} > 500$ GeV
12	$\lvert\Delta\eta_{jj}\rvert > 2.4$
13	$\eta_{j_1} \times \eta_{j_2} < 0$
14	lepton centrality $\zeta > -0.5$
15	$f_{\mathrm{recoil}} < 2.0$

Table 2: Kinematic selection criteria used in the signal region.

have $\zeta > -0.5$. The centrality variable [16] is defined as $\zeta = \min(\eta_1^{jet} - \eta_1^{\ell},\ \eta_2^{jet} - \eta_2^{\ell})$, where the leptons and jets are ordered such that $\eta_1^{\ell} \geq \eta_2^{\ell}$ and $\eta_1^{jet} \geq \eta_2^{jet}$.

In order to reject the $Z/\gamma^* \to \ell\ell$ background with misreconstructed $E_{\mathrm{T}}^{\mathrm{miss}}$ the variable f_{recoil} [50] is introduced. The two leptons in the $Z \to \ell\ell$ events need to be balanced by a hadronic recoil system. The definition of f_{recoil} is

$$f_{\mathrm{recoil}} = \frac{\left|\sum_{\text{soft jets}} \mathrm{JVT}_j \cdot \vec{p}_{\mathrm{T}}^{\,j}\right|}{p_{\mathrm{T}}^{\ell\ell}}, \tag{1}$$

where $p_{\mathrm{T}}^{\ell\ell}$ is the transverse momentum of the dilepton system, $\vec{p}_{\mathrm{T}}^{\,j}$ is the transverse momentum of the $j-$th soft recoil jet. This variable measures the strength of the recoil system relative to the dilepton system, with the p_{T} of the soft jets weighted by JVT to reduce the effects of soft jets from pile-up. The soft recoil system is reconstructed as the vector sum $\vec{p}_{\mathrm{T}}$ of soft jets with $p_{\mathrm{T}} > 10$ GeV and $\lvert\eta\rvert < 4.5$ in the transverse quadrant opposite the dilepton system. Events are required to have $f_{\mathrm{recoil}} < 2.0$.

These selection criteria are applied for five resonance types and masses considered. The signal acceptance times efficiency is in the range of 5% – 22% depending on the mass and type of resonance and the decay channel.

5 Background Estimation

The SM backgrounds come from two sources: (1) SM processes with two prompt opposite-sign leptons in the final states and (2) SM processes accompanied by jets that are misidentified as isolated leptons.

Contributions from background processes with two prompt opposite-sign leptons in the final state are estimated using MC-simulated events. These processes include top pair production, Wt production, $t\bar{t}V$, Z+jets,diboson, and Higgs production via gluon fusion and VBF. The contributions in the signal region

are normalized according to the production cross sections and the integrated luminosity as described in Section 3. The modelling of these backgrounds are validated in several validation regions described in Section 6.

Processes with a single prompt lepton produced in association with hadronic jets enter the signal region when one jet is misidentified as an isolated lepton. This fake-lepton background mainly originates from W+jets, multijet (including semileptonic decays of $b-$quark pairs) and semileptonic decay of the $t\bar{t}$ processes. Since the probability for a jet to be misidentified as an isolated lepton may not be accurately modelled in the MC simulation, a data-driven technique, called the "matrix method" [51], is employed to estimate this contribution.

The probability for a jet to be misidentified as an isolated muon is found to be small given the muon selection criteria used, thus only jets misidentified as electrons are considered. A looser electron selection criteria is defined in addition to the default selection criteria described in Section 4. For looser electrons, the isolation requirement is dropped and the "loose" identification criteria is used instead of the "tight" identification criteria. The matrix method uses the probabilities for a looser quality electron to pass the default electron selection for both prompt and non-prompt leptons. These two probabilities are called efficiency and fake probability, and are measured in data using $Z \to ee$ events and dijet events.

Lepton efficiency and fake probability are measured as a function of the lepton p_{T} and the measured p_{T} dependence is used to determine the number of fake-lepton background events. The electron average efficiency is found to be around 84% and the average fake probability is found to be 13%. The matrix method is applied on each event and the resulting weights are then summed over all events to obtain the fake-lepton background.

6 Background Validation

With all selection criteria applied, the Z+jets process is the dominant background source in the ee and $\mu\mu$ channels while $t\bar{t}$ is the main background source in the $e\mu$ channel. In the following, the validation of these background estimates is described.

An inclusive Z+jets sample is selected by applying selection requirement #1 to #9, but reversing selection requirement #7 in Table 2, some discrepancy is found between data and MC prediction for the Z boson p_{T} distribution in both ee and $\mu\mu$ channels. This indicates that the Z boson p_{T} is not modelled well with the event generator used. A reweighting function is derived to correct the MC prediction to match with the observed Z boson p_{T} distribution in data. This reweighting function is used for the Z+jets prediction in both validation and signal regions.

Three validation regions (VRs), referred to as the "Z+jets VR","$t\bar{t}$ VR", and "low-m_{jj} VR", are used to validate background predictions. Thee VRs select phase spaces similar to the one corresponding to the signal region, with only one or two selection criteria loosened or inverted. The signal contribution to these VRs are negligible. The selection criteria used for all VRs are listed in Table 3.

The Z+jets VR is used to test the Z+jets background prediction and the dilepton mass is required to be within 25 GeV of the Z boson pole mass. The $t\bar{t}$ VR is used to test the $t\bar{t}$ background estimation, and is defined by inverting the b-jet veto criteria to require the presence of at least one b-tagged jet in the event. The m_{jj} selection criteria is dropped in both VRs to obtain more statistics. The low m_{jj} VR is used to

Region	Purpose	Requirements
Z+jets VR	Validate Z+jets background modelling	no m_{jj} cut, $\lvert m_{\ell\ell} - m_Z \rvert < 25$ GeV (only ee and $\mu\mu$ channels)
$t\bar{t}$ VR	Validate $t\bar{t}$ background modelling	no m_{jj} cut, at least one b-tagged jet
low-m_{jj} VR	Validate low-mass background estimation	$m_{jj} < 500$ GeV

Table 3: Definitions of validation regions used, and the requirements listed in Table 2 are assumed unless otherwise specified.

Z+jets VR	ee	$\mu\mu$
Z+jets	808 ± 13 ± 337	1686 ± 20 ± 721
$t\bar{t}$	17.2 ± 0.7 ± 4.5	25.5 ± 0.9 ± 6.2
Wt	1.6 ± 0.2 ± 0.5	2.5 ± 0.2 ± 0.5
diboson_QCD	14.2 ± 1.4 ± 2.6	20.9 ± 1.7 ± 5.4
diboson_EW	0.7 ± 0.0 ± 0.1	0.9 ± 0.1 ± 0.1
$Z\gamma$	29.0 ± 0.9 ± 8.4	48.5 ± 1.2 ± 15.2
Higgs	0.1 ± 0.0 ± 0.3	0.1 ± 0.0 ± 0.0
ttV	0.1 ± 0.0 ± 0.0	0.1 ± 0.0 ± 0.0
fake-lepton	6.9 ± 2.9 ± 1.6	0.0 ± 0.0 ± 0.0
Total background	878 ± 13 ± 347	1784 ± 20 ± 741
Data	804	1630

Table 4: Background estimation and data yields in the Z+jets VR for the ee and $\mu\mu$ channels. The first uncertainty is statistical and the second is systematic.

check the background modelling in a region with similar background composition to the signal region, and is defined by requiring $m_{jj} < 500$ GeV.

Tables 4, 5, and 6 show the number of data events compared to the expectations from signal and various background sources for all three VRs. Good agreement between data and predictions is seen in all regions. Backgrounds from different sources are grouped together. The term "Z+jets" includes both electroweak and strong production of Z+jets processes, "$t\bar{t}$" and "Wt" represent the top pair and single top production, respectively. The term "diboson_QCD" includes strong production of $\ell\ell\nu\nu(WW/ZZ)$, $W(\to qq)Z(\to \ell\ell)$ and $Z(\to qq)Z(\to \ell\ell)$, and "diboson_EW" includes electroweak production of $WWjj$ and $ZZjj$. The term "$Z\gamma$" includes both electroweak and strong production of $Z\gamma jj$, while "$t\bar{t}V$" includes both $t\bar{t}W$ and ttZ contribution. The term "Higgs" includes both gluon-fusion (ggH) and VBF processes.

7 Systematic Uncertainty

Experimental systematic uncertainties on the signal and background yields estimated from MC simulation are derived from uncertainties on object reconstruction and identification efficiency correction factors, energy and momentum scaling and smearing parameters, the $E_{\mathrm{T}}^{\mathrm{miss}}$ modelling, and the b-tagging efficiency/mistag rate, luminosity and trigger efficiency. The dominant uncertainty comes from uncertainties

$t\bar{t}$ VR	ee	$\mu\mu$	$e\mu$
Z+jets	14.1 ± 1.1 ± 5.6	24.6 ± 2.0 ± 8.7	2.8 ± 0.5 ± 1.4
$t\bar{t}$	247 ± 3 ± 24	364 ± 3 ± 35	954 ± 5 ± 92
Wt	17.8 ± 0.6 ± 2.0	26.7 ± 0.8 ± 2.7	64.6 ± 1.2 ± 7.4
diboson_QCD	1.6 ± 0.2 ± 0.4	2.1 ± 0.2 ± 0.5	4.6 ± 0.2 ± 1.0
diboson_EW	0.2 ± 0.0 ± 0.0	0.2 ± 0.0 ± 0.1	0.7 ± 0.0 ± 0.2
$Z\gamma$	1.5 ± 0.2 ± 0.7	1.8 ± 0.2 ± 1.0	0.0 ± 0.0 ± 0.2
Higgs	0.1 ± 0.0 ± 0.0	0.1 ± 0.0 ± 0.0	0.2 ± 0.0 ± 0.1
ttV	0.3 ± 0.0 ± 0.0	0.4 ± 0.0 ± 0.1	0.9 ± 0.0 ± 0.1
fake-lepton	4.0 ± 1.7 ± 0.5	0.0 ± 0.0 ± 0.0	2.2 ± 2.0 ± 0.3
Total background	287 ± 3 ± 29	420 ± 4 ± 40	1030 ± 6 ± 98
Data	279	444	1042

Table 5: Background estimation and data yields in the $t\bar{t}$ VR for the ee, $\mu\mu$ and $e\mu$ channels. The first uncertainty is statistical and the second is systematic.

low-m_{jj} VR	ee	$\mu\mu$	$e\mu$
Z+jets	30 ± 2 ± 13	58 ± 3 ± 24	7 ± 1 ± 2
$t\bar{t}$	21 ± 1 ± 5	30 ± 1 ± 8	73 ± 1 ± 19
Wt	2.4 ± 0.2 ± 0.6	2.9 ± 0.3 ± 0.7	6.8 ± 0.4 ± 1.6
diboson_QCD	3.3 ± 0.3 ± 0.4	5.2 ± 0.3 ± 0.5	13.4 ± 0.4 ± 1.7
diboson_EW	0.0 ± 0.0 ± 0.1	0.3 ± 0.0 ± 0.1	0.6 ± 0.0 ± 0.1
$Z\gamma$	4.3 ± 0.4 ± 1.4	7.1 ± 0.5 ± 2.5	0.1 ± 0.1 ± 0.1
Higgs	0.1 ± 0.0 ± 0.0	0.3 ± 0.0 ± 0.1	0.5 ± 0.0 ± 0.0
ttV	0.0 ± 0.0 ± 0.0	0.0 ± 0.0 ± 0.0	0.1 ± 0.0 ± 0.0
fake-lepton	3.2 ± 1.0 ± 0.1	0.0 ± 0.0 ± 0.0	1.2 ± 0.7 ± 0.1
Total background	64 ± 3 ± 17	103 ± 3 ± 29	103 ± 2 ± 21
Data	51	95	118

Table 6: Background estimation and data yields in the low-m_{jj} VR for the $ee, e\mu$ and $\mu\mu$ channels. The first uncertainty is statistical and the second is systematic.

on jet energy scale (JES) and jet energy resolution (JER). Uncertainties on the Z+jets background due to the Z boson p_{T} reweighting are estimated by varying the fit parameters within their uncertainties. The uncertainty on the fake-lepton background estimate using the matrix method is dominated by prompt-lepton contamination in the dijet sample, the uncertainty on the electron efficiency and fake probability measurements, and the statistical uncertainty on number of data events used in the matrix method. Table 7 summarizes experimental systematic uncertainties for the SM background yield in the signal region. The overall experimental systematic uncertainty is found to be 35%, 31%, and 20% in the ee, $\mu\mu$, and $e\mu$ channels, respectively.

Theoretical uncertainties on the production cross sections of various physics processes with contributions estimated from MC simulation are 20% for Z+jets production [52] [53], 6% for $t\bar{t}$ production [54], 5% for single top quark production [55], 6% for strong production of $WWjj$ [56], 10% for electroweak production of $WWjj$ [56], 5% for WZ [56], 6% for ZZ [56], 4% for $Z\gamma$ [57], 9% for Higgs ggF production [58], 3% for Higgs VBF production [58], 13% for $t\bar{t}W$ [59], and 12% for $t\bar{t}Z$ [59]. Additional shape systematic uncertainties are included for the two dominant background sources. For the Z+jets

Source	ee	$\mu\mu$	$e\mu$
JES and JER	33%	29%	12%
b-tagging	8%	7%	16%
E_T^{miss} modelling	7%	6%	1%
Lepton	3.1%	2.2%	1.5%
Trigger	0.1%	0.5%	0.5%
Matrix method	0.2%	0.0%	0.1%
Z boson p_{T} reweighting	0.5%	0.4%	0.0%
MC statistics	4.1%	3.7%	2.6%
Luminosity	2.1%	2.1%	2.1%
Total experimental uncertainty	35%	31%	20%

Table 7: Summary of experimental systematic uncertainties on the number of predicted SM background events in the signal region.

process, the predicted M_{T}^{WW} shape difference between Sherpa and Madgraph is considered. For the $t\bar{t}$ process, the M_{T}^{WW} shape uncertainty due to hard scatter generation is estimated using Powheg+Herwig++ and aMC@NLO+Herwig++, the uncertainty due to fragmentation and hadronization model is estimated using Powheg+Pythia6 and Powheg+Herwigpp, and the uncertainty due to additional parton radiation is estimated using Powheg+Pythia6 by varying parton shower radiation parameters and scales.

Depending on the resonance type and the pole mass, the overall systematic uncertainty on the signal yield varies from 10% to 70%. The dominant background sources come from uncertainties on JES, JER, $b-$tagging, and $E_{\mathrm{T}}^{\mathrm{miss}}$ modelling.

8 Results

The observed number of events in the signal region is compared to the expected background yield with both statistical and systematic uncertainties in Table 8 for all three channels. Signal yields for all resonance types with a mass of 300 GeV are also shown.

Figure 3 shows the observed transverse mass distribution of the WW system, M_{T}^{WW}, compared to the SM prediction in the signal region for all three channels. The definition of M_{T}^{WW} is as follows:

$$(M_{\mathrm{T}}^{WW})^2 = (P_{\ell_1} + P_{\ell_2} + P^{\mathrm{miss}})(P_{\ell_1} + P_{\ell_2} + P^{\mathrm{miss}}), \tag{2}$$

where P^{miss} is the four vector defined by $(E_{\mathrm{T}}^{\mathrm{miss}}, E_x^{\mathrm{miss}}, E_y^{\mathrm{miss}}, 0)$. This definition is not a transverse mass variable in the classical meaning as it includes the longitudinal momenta of the two visible leptons. It is the sum of four-momenta of the two charged leptons and missing transverse momentum.

No excess is observed in data and 95% CL upper limits are therefore derived on the production cross section times branching ratio for these five new resonances ($\sigma(qq \to Rqq \to \ell^+\nu\ell^-\bar{\nu}qq)$ with $\ell = e, \mu$). Due to limited simulated signal sample size at high mass, a counting experiment is performed using the observed data, SM background and signal events in the signal region. RooFit [60], RooStats [61] and HistFactory [62] are used. A combined likelihood function is constructed from the likelihood functions of each individual channel, given by Poisson distributions describing an event counting experiment for each channel, and global constraints for the set of nuisance parameters $\vec{\alpha}$, which parametrize effects

	ee	$\mu\mu$	$e\mu$
Z+jets	17.6 ± 1.2 ± 11.6	36.6 ± 2.3 ± 19.0	6.7 ± 1.2 ± 1.7
$t\bar{t}$	12.1 ± 0.6 ± 3.2	18.2 ± 0.7 ± 4.6	46.9 ± 1.2 ± 12.1
Wt	1.2 ± 0.2 ± 0.3	1.5 ± 0.2 ± 0.5	3.1 ± 0.3 ± 0.8
diboson_QCD	3.1 ± 0.3 ± 0.5	4.2 ± 0.3 ± 0.7	10.2 ± 0.3 ± 1.6
diboson_EW	1.2 ± 0.1 ± 0.1	1.7 ± 0.1 ± 0.2	3.6 ± 0.1 ± 0.4
$Z\gamma$	2.1 ± 0.3 ± 0.6	3.8 ± 0.3 ± 0.7	0.1 ± 0.0 ± 0.1
Higgs	0.3 ± 0.0 ± 0.1	0.4 ± 0.0 ± 0.1	0.8 ± 0.0 ± 0.1
ttV	0.0 ± 0.0 ± 0.0	0.0 ± 0.0 ± 0.0	0.1 ± 0.0 ± 0.0
fake-lepton	0.6 ± 0.6 ± 0.1	0.0 ± 0.0 ± 0.0	1.3 ± 0.7 ± 0.1
σ (m = 300 GeV)	5.1 ± 0.3 ± 0.6	7.5 ± 0.3 ± 0.9	14.4 ± 0.4 ± 1.9
ϕ (m = 300 GeV)	0.3 ± 0.1 ± 0.2	1.0 ± 0.1 ± 0.4	1.6 ± 0.2 ± 0.4
ρ (m = 300 GeV)	8.0 ± 0.4 ± 1.6	11.7 ± 0.4 ± 1.4	24.1 ± 0.6 ± 3.1
f (m = 300 GeV)	15.6 ± 0.6 ± 1.9	22.6 ± 0.8 ± 1.9	50.4 ± 1.2 ± 3.8
t (m = 300 GeV)	3.3 ± 0.2 ± 0.4	4.7 ± 0.2 ± 0.6	6.9 ± 0.3 ± 1.1
Total background	38.2 ± 1.6 ± 13.9	66.4 ± 2.5 ± 21.6	72.6 ± 1.9 ± 14.8
Data	40	74	86

Table 8: Signal and background yields in the signal region for the ee, $\mu\mu$ and $e\mu$ channels. The first uncertainty is statistical and the second is systematic.

from systematic uncertainties. This treatment allows full accounting of the correlation of systematic uncertainties across various contributions (signal and backgrounds) and across channels.

The expected number of events in channel i is taken as a function of the integrated luminosity ($\mathcal{L}$), the signal efficiency (ε_i), the number of background events estimated ($N_{i,b}$), and the predicted signal cross section in the fiducial region (σ_{sig}), and the signal strength (μ):

$$N_i^{\text{exp}}(\mu, \vec{\alpha}) = \mu \cdot \sigma_{\text{sig}} \cdot \mathcal{L} \cdot \varepsilon_i + \sum_b N_{i,b}. \tag{3}$$

Given the observed number of events N_i^{obs} in data, the combined likelihood function is:

$$L(\mu, \vec{\alpha}) = \prod_{i \in \{ee, \mu\mu, e\mu\}} \text{Pois}\left(N_i^{\text{obs}} | N_i^{\text{exp}}(\mu, \vec{\alpha})\right) \prod_{j \in \text{syst}} g(\alpha'_j | \alpha_j). \tag{4}$$

The term $g(\alpha'_j|\alpha_j)$ represents the set of constraints on $\vec{\alpha}$ from auxiliary measurements α'_j.

The upper limits on the production cross section times branching ratio are calculated from the profile-likelihood-ratio test statistics [63], defined as:

$$t = -2 \ln \left(\frac{L(\mu, \hat{\hat{\vec{\alpha}}}(\mu))}{L(\hat{\mu}, \hat{\vec{\alpha}})} \right), \tag{5}$$

where $\hat{\mu}, \hat{\vec{\alpha}}$ are the values that maximize the likelihood function, and $\hat{\hat{\vec{\alpha}}}(\mu)$ are the values of $\vec{\alpha}$ which maximize the likelihood function given at a certain value of μ. The upper limits on μ can be expressed as 95% CL limit on the production cross section times branching ratio (σ), using $\sigma = \mu \times \sigma_{\text{sig}}$.

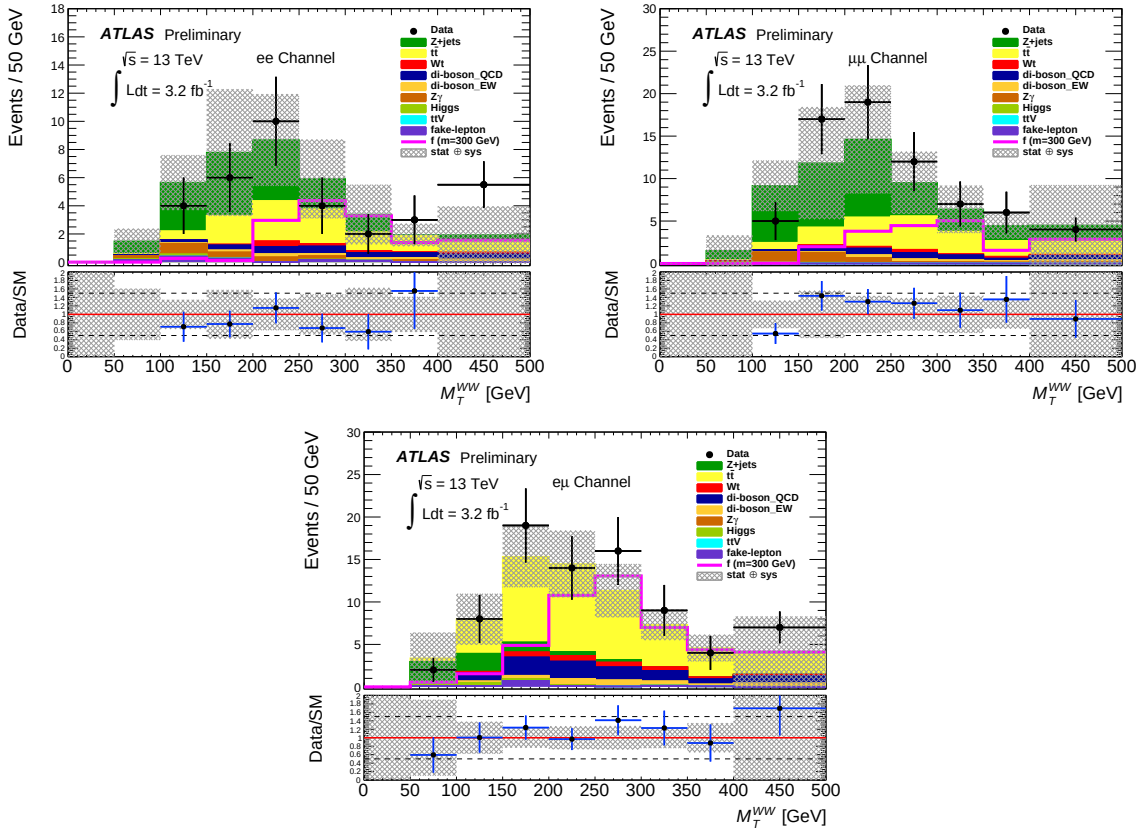

Figure 3: Observed and predicted M_{T}^{WW} distribution in the ee, $\mu\mu$, and $e\mu$ channels in the signal region. The distribution for the f resonance with m = 300 GeV is also shown. The hatching indicates the overall uncertainty on the SM predictions. The lower plot for each decay mode shows the ratio of the data to the SM backgrounds. The hatching represents the overall uncertainty on the ratio. The last bin includes overflow events.

Figure 4 shows the expected and observed limits at 95% CL as a function of the resonance mass, together with the ±1 and ±2 standard deviation uncertainty bands. The observed limits are found to be in the range of 380 – 220 fb for the σ particle, 460 – 240 fb for the ϕ particle, 330 – 270 fb for the ρ particle, 340 – 260 fb for the f particle, and 310 – 260 fb for the t particle. These limits are for the resonance mass in the range of 200 – 500 GeV. With a coupling of 2.5 to longitudinal vector bosons, ρ (f) particles with a mass below 230 (300) GeV are excluded at 95% CL.

9 Conclusion

Studies of vector boson fusion above the Higgs boson mass are important for a better understanding of the electroweak symmetry breaking mechanism. A search was performed for heavy neutral resonances produced through vector boson fusion $qq \to Rqq \to \ell^+\nu\ell^-\bar{\nu}qq$ ($\ell = e, \mu$) using 3.2 fb^{-1} of data at $\sqrt{s}$ = 13 TeV recorded by the ATLAS detector at the LHC. No excess above the SM background expectation is observed. First sets of limits are obtained on the production cross section times branching ratio of five types of new resonances of different spin and isospin (scalar isoscalar, scalar isotensor, vector

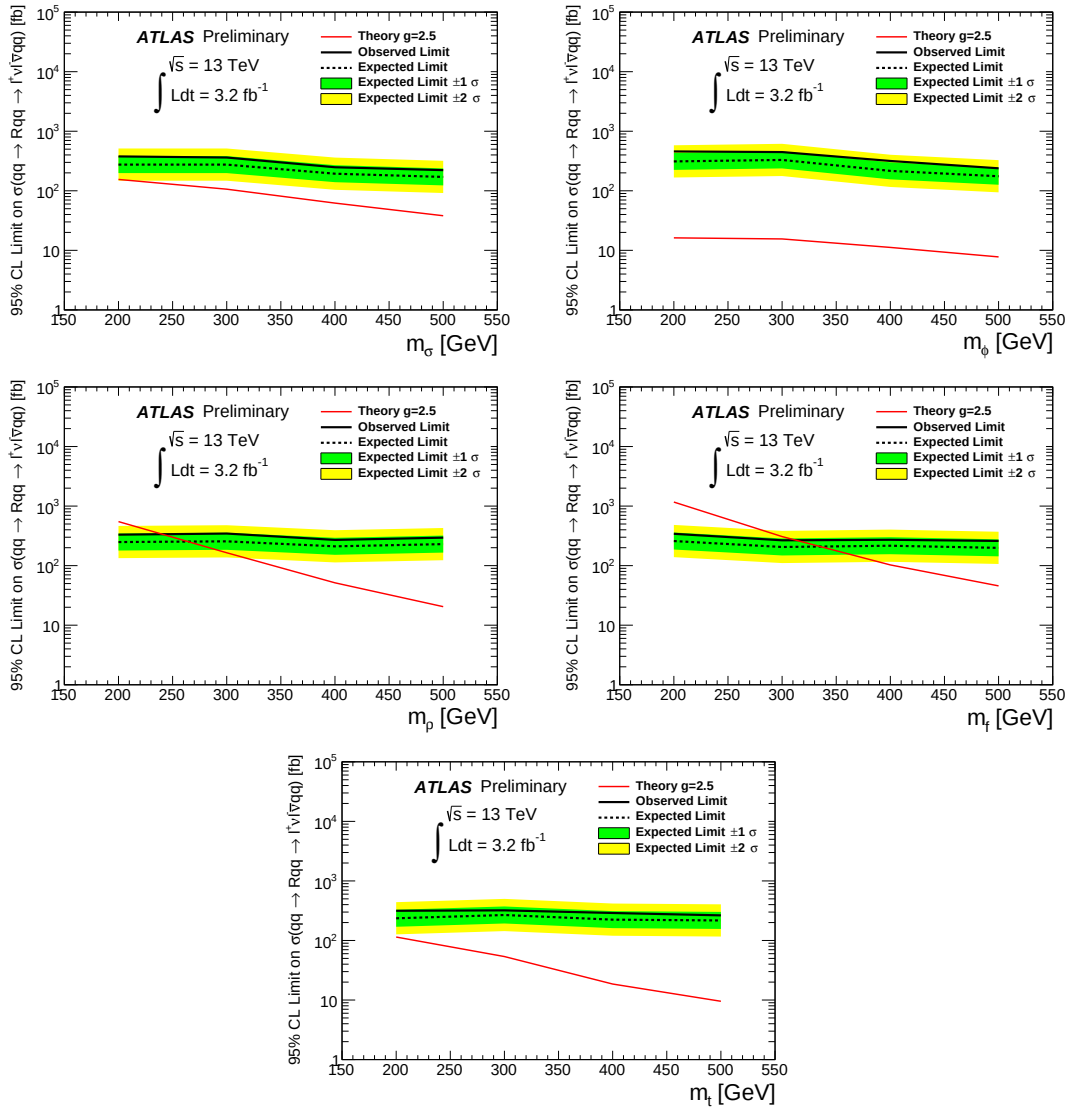

Figure 4: Expected and observed 95% C.L. upper limits on the σ, ϕ, ρ, f and t production cross section times branching ratio, $\sigma(qq \to Rqq \to \ell^+\nu\ell^-\bar{\nu}qq)$ with $\ell = e, \mu$, as a function of its mass. The expected limits are plotted with the ± 1 and ± 2 standard deviation uncertainty bands.

isovector, tensor isoscalar and tensor isotensor) with K-matrix unitarization of the vector boson scattering process. The observed cross section limits are found to be in the range of 460 − 220 fb for resonance masses from 200 to 500 GeV. For an assumed coupling of 2.5 to longitudinal vector bosons, $\rho\,(f)$ particles with a mass below 230 (300) GeV are excluded at 95% CL.

References

[1] M. J. Dugan, H. Georgi and D. B. Kaplan, *Anatomy of a Composite Higgs Model*, Nucl. Phys. **B254** (1985) 299.

[2] K. Agashe, R. Contino and A. Pomarol, *The Minimal composite Higgs model*, Nucl. Phys. **B719** (2005) 165, arXiv: hep-ph/0412089 [hep-ph].

[3] J. F. Gunion et al., *Higgs Bosons in Left-Right Symmetric Models*, Phys. Rev. **D40** (1989) 1546.

[4] M. S. Chanowitz and M. Golden, *Higgs Boson Triplets With $M_W = M_Z \cos\theta_\omega$*, Phys. Lett. **B165** (1985) 105.

[5] J. F. Gunion, R. Vega and J. Wudka, *Higgs triplets in the standard model*, Phys. Rev. **D42** (1990) 1673.

[6] L. Randall and R. Sundrum, *A Large mass hierarchy from a small extra dimension*, Phys. Rev. Lett. **83** (1999) 3370, arXiv: hep-ph/9905221 [hep-ph].

[7] H. Davoudiasl, J. L. Hewett and T. G. Rizzo, *Experimental probes of localized gravity: On and off the wall*, Phys. Rev. **D63** (2001) 075004, arXiv: hep-ph/0006041 [hep-ph].

[8] D. Espriu and B. Yencho, *Longitudinal WW scattering in light of the Higgs boson discovery*, Phys. Rev. **D87** (2013) 055017, arXiv: 1212.4158 [hep-ph].

[9] D. Espriu and F. Mescia, *Unitarity and causality constraints in composite Higgs models*, Phys. Rev. **D90** (2014) 015035, arXiv: 1403.7386 [hep-ph].

[10] W. Kilian et al., *High-Energy Vector Boson Scattering after the Higgs Discovery*, Phys. Rev. **D91** (2015) 096007, arXiv: 1408.6207 [hep-ph].

[11] M. Szleper, *The Higgs boson and the physics of WW scattering before and after Higgs discovery*, (2014), arXiv: 1412.8367 [hep-ph].

[12] A. Dobado, F.-K. Guo and F. J. Llanes-Estrada, *Production cross section estimates for strongly-interacting Electroweak Symmetry Breaking Sector resonances at particle colliders*, Commun. Theor. Phys. **64** (2015) 701, arXiv: 1508.03544 [hep-ph].

[13] T. Appelquist and G.-H. Wu, *The Electroweak chiral Lagrangian and new precision measurements*, Phys.Rev. **D48** (1993) 3235, arXiv: hep-ph/9304240 [hep-ph].

[14] W. Kilian, *Electroweak symmetry breaking: The bottom-up approach*, Springer Tracts Mod. Phys. **198** (2003) 1.

[15] A. Alboteanu, W. Kilian and J. Reuter, *Resonances and Unitarity in Weak Boson Scattering at the LHC*, JHEP **11** (2008) 010, arXiv: 0806.4145 [hep-ph].

[16] J. Schumacher, 'Sensitivity of ATLAS to Alternative Mechanisms of Electroweak Symmetry Breaking in Vector Boson Scattering $qq \to qq\ell\nu\ell\nu$', PhD thesis: TU Dresden, 2010, URL: http://inspirehep.net/record/886924/files/CERN-THESIS-2010-140.pdf.

[17] W. Kilian et al., *Resonances at the LHC beyond the Higgs boson: The scalar/tensor case*, Phys. Rev. **D93** (2016) 036004, arXiv: 1511.00022 [hep-ph].

[18] ATLAS Collaboration,
Observation and measurement of Higgs boson decays to WW^* with the ATLAS detector,
Phys. Rev. D **92** (2015) 012006, arXiv: 1412.2641 [hep-ex].

[19] CMS Collaboration, *Measurement of Higgs boson production and properties in the WW decay channel with leptonic final states*, JHEP **1401** (2014) 096, arXiv: 1312.1129 [hep-ex].

[20] ATLAS Collaboration, *Search for a Charged Higgs Boson Produced in the Vector-Boson Fusion Mode with Decay $H^{\pm} \to W^{\pm}Z$ using pp Collisions at $\sqrt{s} = 8$ TeV with the ATLAS Experiment*, Phys. Rev. Lett. **114** (2015) 231801, arXiv: 1503.04233 [hep-ex].

[21] ATLAS Collaboration, *The ATLAS Experiment at the CERN Large Hadron Collider*, JINST **3** (2008) S08003.

[22] W. Kilian, T. Ohl and J. Reuter, *WHIZARD: Simulating Multi-Particle Processes at LHC and ILC*, Eur.Phys.J. **C71** (2011) 1742, arXiv: 0708.4233 [hep-ph].

[23] J. Reuter et al., *Modern Particle Physics Event Generation with WHIZARD*, J. Phys. Conf. Ser. **608** (2015) 012063, arXiv: 1410.4505 [hep-ph].

[24] T. Sjostrand, S. Mrenna and P. Z. Skands, *A Brief Introduction to PYTHIA 8.1*, Comput. Phys. Commun. **178** (2008) 852, arXiv: 0710.3820 [hep-ph].

[25] J. Pumplin et al.,
New generation of parton distributions with uncertainties from global QCD analysis,
JHEP **07** (2002) 012, arXiv: hep-ph/0201195 [hep-ph].

[26] ATLAS Collaboration, *ATLAS Pythia 8 tunes to 7 TeV data*, ATL-PHYS-PUB-2014-021, 2014, URL: http://cdsweb.cern.ch/record/1966419.

[27] S. Alioli et al., *A general framework for implementing NLO calculations in shower Monte Carlo programs: the POWHEG BOX*, JHEP **1006** (2010) 043, arXiv: 1002.2581 [hep-ph].

[28] H.-L. Lai et al., *New parton distributions for collider physics*, Phys.Rev. **D82** (2010) 074024, arXiv: 1007.2241 [hep-ph].

[29] T. Sjostrand, S. Mrenna and P. Z. Skands, *PYTHIA 6.4 Physics and Manual*, JHEP **05** (2006) 026, arXiv: hep-ph/0603175 [hep-ph].

[30] M. Czakon and A. Mitov,
Top++: A Program for the Calculation of the Top-Pair Cross-Section at Hadron Colliders,
Comput. Phys. Commun. **185** (2014) 2930, arXiv: 1112.5675 [hep-ph].

[31] J. Alwall et al., *The automated computation of tree-level and next-to-leading order differential cross sections, and their matching to parton shower simulations*, JHEP **07** (2014) 079, arXiv: 1405.0301 [hep-ph].

[32] R. D. Ball et al., *Parton distributions with LHC data*, Nucl. Phys. **B867** (2013) 244, arXiv: 1207.1303 [hep-ph].

[33] M. V. Garzelli et al., *Z0 - boson production in association with a top anti-top pair at NLO accuracy with parton shower effects*, Phys. Rev. **D85** (2012) 074022, arXiv: 1111.1444 [hep-ph].

[34] S. Catani et al.,
Vector boson production at hadron colliders: a fully exclusive QCD calculation at NNLO,
Phys. Rev. Lett. **103** (2009) 082001, arXiv: 0903.2120 [hep-ph].

[35] R. Gavin et al., *FEWZ 2.0: A code for hadronic Z production at next-to-next-to-leading order*, Comput. Phys. Commun. **182** (2011) 2388, arXiv: 1011.3540 [hep-ph].

[36] K. Melnikov and F. Petriello, *Electroweak gauge boson production at hadron colliders through $O(\alpha_s^2)$*, Phys. Rev. **D74** (2006) 114017, arXiv: hep-ph/0609070 [hep-ph].

[37] T. Gleisberg et al., *Event generation with SHERPA 1.1*, JHEP **02** (2009) 007, arXiv: 0811.4622 [hep-ph].

[38] B. Jager, C. Oleari and D. Zeppenfeld, *Next-to-leading order QCD corrections to Z boson pair production via vector-boson fusion*, Phys. Rev. **D73** (2006) 113006, arXiv: hep-ph/0604200 [hep-ph].

[39] G. Bozzi et al., *Next-to-leading order QCD corrections to W^+Z and W^-Z production via vector-boson fusion*, Phys. Rev. **D75** (2007) 073004, arXiv: hep-ph/0701105 [hep-ph].

[40] S. Agostinelli et al., *GEANT4: A Simulation toolkit*, Nucl. Instrum. Meth. **A506** (2003) 250.

[41] ATLAS Collaboration, *The ATLAS Simulation Infrastructure*, Eur. Phys. J. C **70** (2010) 823, arXiv: 1005.4568 [hep-ex].

[42] ATLAS Collaboration, *Electron efficiency measurements with the ATLAS detector using the 2012 LHC proton–proton collision data*, ATLAS-CONF-2014-032, 2014, URL: http://cdsweb.cern.ch/record/1706245.

[43] ATLAS Collaboration, *Electron identification measurements in ATLAS using $\sqrt{s}$ = 13 TeV data with 50 ns bunch spacing*, ATLAS-PHYS-PUB-2015-041, 2015, URL: http://cdsweb.cern.ch/record/2048202.

[44] ATLAS Collaboration, *Muon reconstruction performance of the ATLAS detector in proton-proton collision data at $\sqrt{s}$ = 13 TeV*, Eur. Phys. J. **C76** (2016) 292, arXiv: 1603.05598 [hep-ex].

[45] M. Cacciari, G. P. Salam and G. Soyez, *The Anti-k_t jet clustering algorithm*, JHEP **04** (2008) 063, arXiv: 0802.1189 [hep-ph].

[46] ATLAS Collaboration, *Jet energy measurement and its systematic uncertainty in proton–proton collisions at $\sqrt{s}$ = 7 TeV with the ATLAS detector*, Eur. Phys. J. C **75** (2015) 17, arXiv: 1406.0076 [hep-ex].

[47] ATLAS Collaboration, *Jet global sequential corrections with the ATLAS detector in proton–proton collisions at $\sqrt{s}$ = 8 TeV*, ATLAS-CONF-2015-002, 2015, URL: http://cdsweb.cern.ch/record/2001682.

[48] ATLAS Collaboration, *Tagging and suppression of pileup jets with the ATLAS detector*, ATLAS-CONF-2014-018, 2014, URL: http://cdsweb.cern.ch/record/1700870.

[49] ATLAS Collaboration, *Expected performance of the ATLAS btagging algorithms in Run 2*, ATLAS-PHYS-PUB-2015-022, 2015, URL: http://cdsweb.cern.ch/record/2037697.

[50] ATLAS Collaboration, *Observation and measurement of Higgs boson decays to WW^* with the ATLAS detector*, Phys. Rev. **D92** (2015) 012006, arXiv: 1412.2641 [hep-ex].

[51] ATLAS Collaboration, *Search for high-mass dilepton resonances in pp collisions at $\sqrt{s}$ = 8 TeV with the ATLAS detector*, Phys. Rev. D **90** (2014) 052005, arXiv: 1405.4123 [hep-ex].

[52] ATLAS Collaboration, *Measurement of the production cross sections of a Z boson in association with jets in collisions at* $\sqrt{s} = 13$ *TeV with the ATLAS detector*, URL: https://atlas.web.cern.ch/Atlas/GROUPS/PHYSICS/CONFNOTES/ATLAS-CONF-2015-041/.

[53] ATLAS Collaboration, *Measurement of the electroweak production of dijets in association with a Z-boson and distributions sensitive to vector boson fusion in proton-proton collisions at* $\sqrt{s} = 8$ *TeV using the ATLAS detector*, JHEP **04** (2014) 031, arXiv: 1401.7610 [hep-ex].

[54] M. Czakon and A. Mitov,
Top++: A Program for the Calculation of the Top-Pair Cross-Section at Hadron Colliders,
Comput. Phys. Commun. **185** (2014) 2930, arXiv: 1112.5675 [hep-ph].

[55] N. Kidonakis,
Two-loop soft anomalous dimensions for single top quark associated production with a W^- *or* H^-,
Phys. Rev. **D82** (2010) 054018, arXiv: 1005.4451 [hep-ph].

[56] ATLAS Collaboration, *Evidence for Electroweak Production of* $W^\pm W^\pm jj$ *in pp Collisions at* $\sqrt{s} = 8$ *TeV with the ATLAS Detector*, Phys. Rev. Lett. **113** (2014) 141803,
arXiv: 1405.6241 [hep-ex].

[57] ATLAS Collaboration,
Measurements of $Z\gamma$ *and* $Z\gamma\gamma$ *production in pp collisions at* $\sqrt{s} = 8$ *TeV with the ATLAS detector*,
Phys. Rev. **D93** (2016) 112002, arXiv: 1604.05232 [hep-ex].

[58] ATLAS and CMS Collaborations, *SM Higgs production cross sections at* $\sqrt{s} = 13 - 14$ *TeV*,
CERNYellowReportPageAt1314TeV2014, Geneva, 2016, URL: https://twiki.cern.ch/twiki/bin/view/LHCPhysics/CERNYellowReportPageAt1314TeV2014.

[59] ATLAS Collaboration, *Measurement of the* $t\bar{t}Z$ *and* $t\bar{t}W$ *production cross sections in multilepton final states using* 3.2 fb^{-1} *of pp collisions at* 13 *TeV at the LHC*, ATLAS-CONF-2016-003, 2016,
URL: http://cdsweb.cern.ch/record/2138947.

[60] W. Verkerke and D. P. Kirkby, *The RooFit toolkit for data modeling*,
eConf **C0303241** (2003) MOLT007, [,186(2003)], arXiv: physics/0306116 [physics].

[61] L. Moneta et al., *The RooStats Project*, (2010), arXiv: 1009.1003.

[62] K. Cranmer et al.,
HistFactory: A tool for creating statistical models for us with RooFit and RooStats,
URL: https://cds.cern.ch/record/1456844/.

[63] ATLAS and CMS Collaborations,
Procedure for the LHC Higgs boson search combination in summer 2011,
URL: https://cds.cern.ch/record/1375842/.